Digital elevation model generation using UAV-SfM photogrammetry techniques to map sea-level rise scenarios at Cassino Beach, Brazil

Deivid Cristian Leal-Alves[1] · Jair Weschenfelder[1] · Miguel da Guia Albuquerque[2] · Jean Marcel de Almeida Espinoza[3] · Marlize Ferreira-Cravo[4] · Luis Pedro Melo de Almeida[5]

Abstract

The Cassino Beach is a low-lying coast with high inundation susceptibility in southern Brazil. To map this vulnerability, a low cost alternative to the increasingly employed fine-scale remote sensing is the employment of a digital camera coupled with unmanned aerial vehicle (UAV). However, this was only achieved through the adoption of photogrammetric principles and computational advances of structure-from-motion (SfM) algorithms. The study objectives were: a topographic reconstruction of the Cassino beach; an accurate digital terrain model (DTM) generation from the dense cloud classification; and inundation maps based on representative concentration pathway (RCP) scenarios from the Intergovernmental Panel on Climate Change using the bathtub approach. The primary input of the inundation model was a DTM with spatial resolution of 0.1294 m and an RMSE elevation of 0.0607 m. The high-resolution and vertical precision were appropriated to the bathtub approach, with the mapping identifying the exposed areas with the drowning potential correctly connected to the source. The inundation maps revealed that: in the 2046–2065 RCP scenario, the urban drowned area has varied between 37 and 41%; in the 2081–2100 RCP scenario, the urban drowned area has varied between 51 and 73%; and in the 2100 RCP scenario, the urban drowned area has varied between 54 and 82%. The bathtub modeling shows that low-lying coasts are highly susceptible to sea-level rise effects, and the use of UAV-SfM technology in the production of topographic data was suitable for the study area.

Keywords Coastal geomorphology · Unmanned aerial vehicle · Coastline benchmark · Climate change · Bathtub approach

1 Introduction

High-resolution digital elevation models (DEMs) are widely used as primary topographic input for coastal inundation assessment [1, 2]. In computational hydrological modeling, the geomorphometry parameters derived from DEMs are essential for drainage network extraction, flow identification, streams connectivity, and application of various flooding approaches [3–6]. Until recently, access to high-resolution DEMs was restricted to costly aerial

✉ Deivid Cristian Leal-Alves, dclealalves@gmail.com; Jair Weschenfelder, jair.weschenfelder@ufrgs.br; Miguel da Guia Albuquerque, miguel.albuquerque@riogrande.ifrs.edu.br; Jean Marcel de Almeida Espinoza, jean.espinoza@ifsc.edu.br; Marlize Ferreira-Cravo, lizedomar@gmail.com; Luis Pedro Melo de Almeida, melolp@gmail.com | [1]Pós-Graduação em Geociências, Universidade Federal do Rio Grande do Sul – UFRGS, Av. Bento Gonçalves, 9500 Prédio 43113 Sala 207 (Bloco I) Bairro Agronomia, CEP 91501-970, Porto Alegre, Rio Grande do Sul, Brazil. [2]Instituto Federal de Educação, Ciência e Tecnologia do Rio Grande do Sul – IFRS, Campus Rio Grande, Rua Engenheiro Alfredo Huch, 475, Bairro Centro, CEP 96201-460, Rio Grande, Rio Grande do Sul, Brasil. [3]Instituto Federal de Educação, Ciência e Tecnologia de Santa Catarina – IFSC Campus Caçador, Avenida Fahdo Thomé, 3000, Bairro Champagnat, CEP 89500-000, Caçador – SC, Brazil. [4]Instituto Federal do Paraná – IFPR Campus Paranaguá, Rua Antônio Carlos Rodrigues, 453, Bairro Porto Seguro, CEP 83215-750, Paranaguá, Paraná, Brasil. [5]Universidade Federal do Rio Grande – FURG, Av. Itália, km 8 – Bairro Carreiros, CEP 96203-900, Rio Grande, Rio Grande do Sul, Brasil.

surveys of light detection and ranging (LiDAR) systems. However, the use of unmanned aerial vehicle (UAV) platforms has proven to be a high-performance alternative for topographic surveys due to the emerging areas such as computing embedded, robotics, and geomatics [7]. The rapid advancement in on-board technology has provided greater flexibility and reliability for UAV surveys, with lower operating costs and agile data acquisition and processing [8–11]. These elements have popularized the use of UAV platforms in a variety of civil society activities (agriculture, architecture, engineering, transportation, risk management) and consolidate it as a tool in geosciences [12, 13].

UAVs carrying small-format digital cameras can reconstruct topographic surveys using the structure-from-motion (SfM) algorithm [10, 14]. However, for UAV-SfM-derived DEMs to be technically reliable, the unrestricted adoption of photogrammetric principles in flight planning steps is required; proper calibration of the aircraft (especially the inertial unit and navigation system); and optimizing camera settings according to the particulars of the environment and geomorphology that will be photographed [12, 15, 16]. As with LiDAR technology, the vertical quality of UAV-SfM derived DEMs still depend on the use of GNSS-RTK receivers to acquire ground control points (GCPs), ensuring centimeter precision in photogrammetric bundle block adjustment [9, 16]. The combination of high-resolution DEMs supported by GNSS-RTK receivers, either on ground targets or on-board the platform, has led to a significant increase in research addressing accurate sea-level rise (SLR) impact assessment, especially in low-lying coastal areas [5, 17–19].

The SLR is one of the significant challenges of coastal management in the coming decades. The twentieth century has experienced an increasing temperature variability, with significant intensification in the last four decades [20], and several models indicate that these rates will increase in the twenty-first century due to the effects of global warming [21]. The negative balance of ice mass in Greenland [22] and west Antarctic [23], as well as the linear trend of decrease seasonal Arctic sea ice extent detected by satellite monitoring [24], amplifies the complexity of climate modeling because these factors can represent changes patterns of ocean and atmospheric circulation. According to IPCC projections, by the end of the twenty-first century, most likely around 70% of coastlines will experience a change in local sea level of approximately 20% of the global average, which is much more critical in regions with low topography [20, 25] For Nicholls et al. [26], SLR due to global warming seems inevitable, but the rates and geographic patterns of such changes remain uncertain. However, even with the uncertainties inherent in climate systems modeling, predictions about SLR are essential tools for assessing coastal inundation vulnerability [17, 26].

The bathtub model is a recurring approach for coastal inundation assessments [2, 5, 6, 17–19]. Consisting in a 2D hydrostatic geospatial method that employs DEMs to simulate water flows, its structure is strongly dependent on the quality of the topographic input data [2, 17]. The model is mainly used for potential inundation mapping assessment in coastal areas [18]. The bathtub approach allows simulating water levels by extracting information such as the extent of drowned areas and their water height. These maps can assist in the planning of mitigation measures in the face of climate change impacts [2]. The bathtub approach is especially valid for low-lying coastal environments with high susceptibility to positive sea-level fluctuations [25].

This paper presents the results of a coastal inundation modeling using the UAV-SfM-derived DEM in the southernmost of Brazil. The study area comprises Cassino Beach, a low-lying prograded barrier with coastal streams that increase the susceptibility of the hinterland urban area to inundation [27, 28]. The National Policy on Climate Change reports [29] and the Brazilian Panel on Climate Change [30] highlight that Brazil's southern coast is one of the most exposed to high-energy events, such as those caused by storm surge from extratropical cyclogenesis. The main objective was accurate topographic reconstruction using digital photogrammetric techniques and SfM processing for use in sea-level rise modeling. The bathtub model was employed according to the methodology proposed by the National Oceanic and Atmospheric Administration [31], fully implemented through a geographic information system (GIS). The modeled SLR values were based on the four representative concentration pathway scenarios of the intergovernmental panel on climate change [20], covering 36 estimative projections.

2 Materials and methods

2.1 Study area

The UAV survey was conducted in the Cassino Beach, a low-lying coastal plain located south of the Patos Lagoon inlet, State of Rio Grande do Sul, southernmost Brazil, as shown in Fig. 1. The Rio Grande do Sul Coastal Plain is a 760-km-long plain established by the lateral coalescence of four barrier-lagoon depositional systems [32]. The youngest system (Holocene barrier), the geologic substrate of the study area, is a progradational strand plain developed between 7 and 6 ka with morphogenesis associated with Pleistocene and Holocene marine transgression–regression cycles [32, 33]. The sandy barrier composes a depositional system in the form of foredune ridges, strongly influenced by an abundant sedimentary

Fig. 1 Study area location map
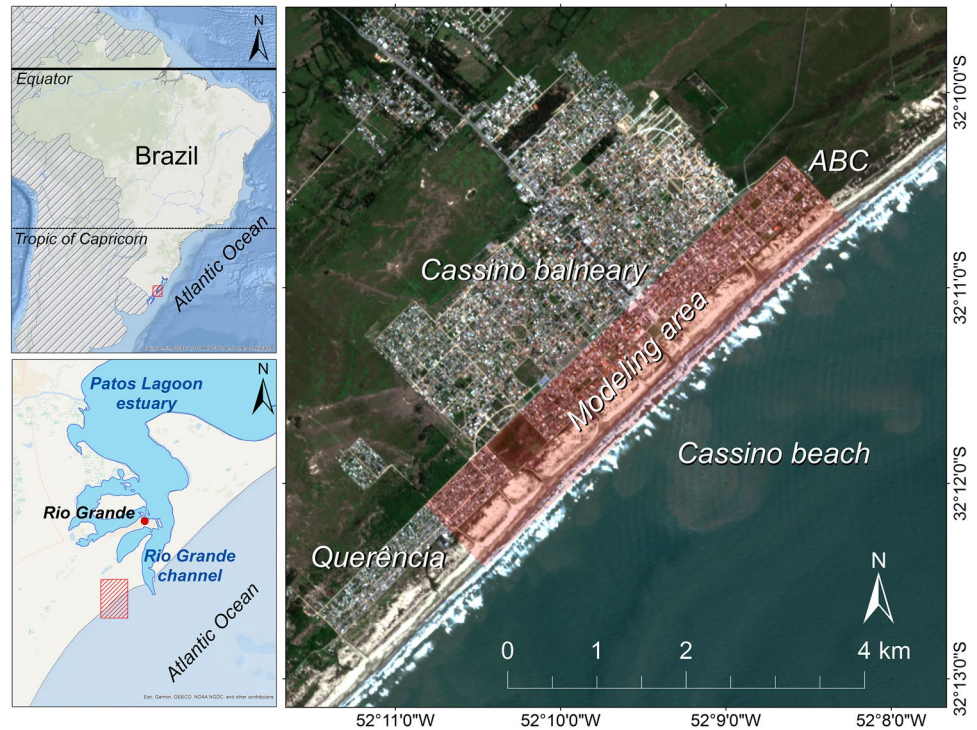
budget of fine- to very-fine-grained sands, as well as the aeolian transport promoted by the action of winds from the northeast quadrant [32–33]. The coastal deposition result is a sandy terrain of smooth transition between the inland alluvial plain and a broad, relatively shallow, low-sloping continental shelf [35, 36].

The coast of Rio Grande do Sul presents a semidiurnal micro-tidal regime, with maximum values not exceeding 0.5 m [32, 34]. It is an exposed wave-dominated coast, where sediment transport is controlled by the action of waves from the southern quadrant, with northeast long-shore drifting [37]. The Cassino Beach morphodynamics is predominantly dissipative, with a low-slope and wide profile composed of a multi-sandbar system [34, 38, 39]. The beach-dune system presents two seasonalities: an erosive profile, associated with the activity of storms originated from the South Atlantic extratropical cyclogenesis, being responsible for the main scarps of the dune base and storm surge flooding, acting in the autumn, winter, and early spring months [38, 40–43], and another of accretion, with the coastal vegetation germination (*Blutaparon portulacoides*) in the spring and summer months, with the formation of ephemeral dune mounds (seasonal cycle) in the backshore called embryonic dunes [44].

Even though the Cassino Beach has large foredune ridges, with a setback of approximately 200 m, the sectioning of the dunefield by streams (regionally known as 'washouts'), and beach access roads facilitate the entry of oceanic waters during episodes of the high-level sea caused by storms [27, 28]. The washouts drain the waters of the coastal plain interior toward the beach system, breaching the foredune ridges. As well as the beach profile variation, the washouts dynamics have an active seasonal component, with flow occurrence and intensification in the shore during periods of higher winter precipitation of the subtropical climate [27]. Serpa et al. [28] point out that the occurrence of washouts increases the susceptibility of the coastal plain to storm surges.

The Cassino Beach urban area has approximately 976 hectares, with over 16,000 inhabitants [45]. The area population tends to increase significantly in the summer months due to intense tourist activity. Between the 1940s and 2000s, the urban area of the Cassino grew about eight-fold [46], a process that has intensified over the past two decades in the range close to the active foredune ridges. Considering only the southern portion, Leal Alves [47] identified an increase of 80% of the built area between the years 2002 and 2012. Lélis [46] also points out that most of the dunes that form the urban site were flatten during the 1970s. A recovery and management plan that began in the 1980s was required to restore the part of the foredune ridges, which is a natural protection to minimize the effects of storm surges and sea-level rise [48].

2.2 UAV and GNSS data acquisition

A DJI Phantom 4 Pro (PH4P) was used for capturing aerial images. This UAV system is composed of a multi-rotor

aircraft (quad) and radio control station (RC). The aircraft weighs 1.4 kg and is powered by a four-cell LiPO battery with an autonomy of approximately 25 min, varying with wind conditions. The remote-sensing payload of the PH4P is a 20-megapixel small-format digital camera CMOS/FC6310 attached to a gimbal (which allows the nadir vertical view) and a stabilizer support that lessened the effects of vibrations during the flight. The images are captured in JPEG format (RGB compositing), with coordinates from an on-board global positioning system receiver (GPS). All survey data are stored on a microSD card embedded in the aircraft. A smartphone was coupled to the RC station to assist the flight operation, which allowed the telemetry to be viewed simultaneously to the flight, in addition to managing route plans through a specialized mobile application.

The aircraft's navigation sensors and inertial measurement unit (IMU) were calibrated, and camera configurations were adjusted as recommended in detail by O'Connor et al. [12]. In order to minimize the effects of solar angulation, the mission schedule preferably comprised the local window from 10 a.m. to 2 p.m. (UTC-3). Since the coastal landscape has mostly silica sands composed of quartz, which gives it a high capacity to reflect the sun's rays, and the chosen time for the survey is close to the local solar zenith, the camera's photosensitive (ISO) was adjusted with value 100, with shutter speed and aperture optimized with values of 1/800 s and f/6.3, respectively. The weather forecast was consulted before each aerial survey day, as well as the on-site conditions before the flight execution through the Instituto Nacional de Meteorologia (INMET) page and ground hand anemometer. Winds with intensity greater than 19.5 kt, high cloudiness, precipitation, or intense sea agitation made the survey impossible. While high winds and precipitation hinder aircraft operation, heavy cloud cover and marine fog impair the images taking [7, 8, 16, 49]. All surveys were performed with the aircraft within the pilot's visual line of sight (VLOS).

The aerial images were captured through 14 low-altitude flight plans between June and October 2018, forming a bundle of 3155 images covering 424.81 hectares of urbanized coast, foredune ridges, shore, and traffic lanes adjacent to the sea. On average, 225 waypoints (center of perspective and coordinate record) were acquired per plane. The flight plans were prepared using the DroneDeploy mapping platform based on the following parameters: flight height of 100 m; 80% frontal overlap; 60% side overlap; gimbal in nadir position; flight line orientation parallel to the coastline (130°–140°); and travel speed between 8 and 10 m/s. The flights were carried out between late winter and early spring according to the viability imposed by the weather conditions, with the five

Table 1 UAV flight plan settings

| Parameter	Value/rating
Total flight plans executed	14
Flight height (meters)	100
Flight time interval (local time)	10 a.m. to 2 p.m
Average flight time per plane (minutes)	18
Average wind conditions (knots)	12
Mapping flight speed (meters per second)	8 to 10
Image overlap (frontal/side percentage)	80/60
ISO configuration	100
Shutter speed	1/800 s
Aperture optimized	f/6.3
Total images acquired	3155
Average waypoints per flight plan	225
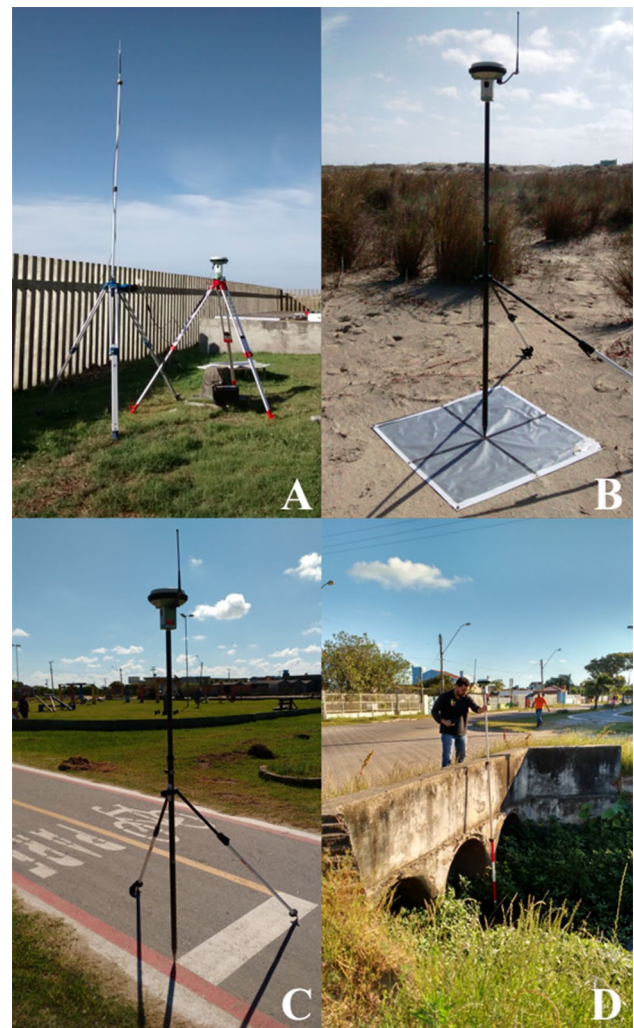
Fig. 2 GNSS-RTK survey. **a** base antenna; **b** GCP survey on target; **c** survey of GCP in bike lane; **d** road culvert coordinate survey

Fig. 3 Workflow of UAV-SfM and GNSS-RTK data acquisition, processing, and verification steps
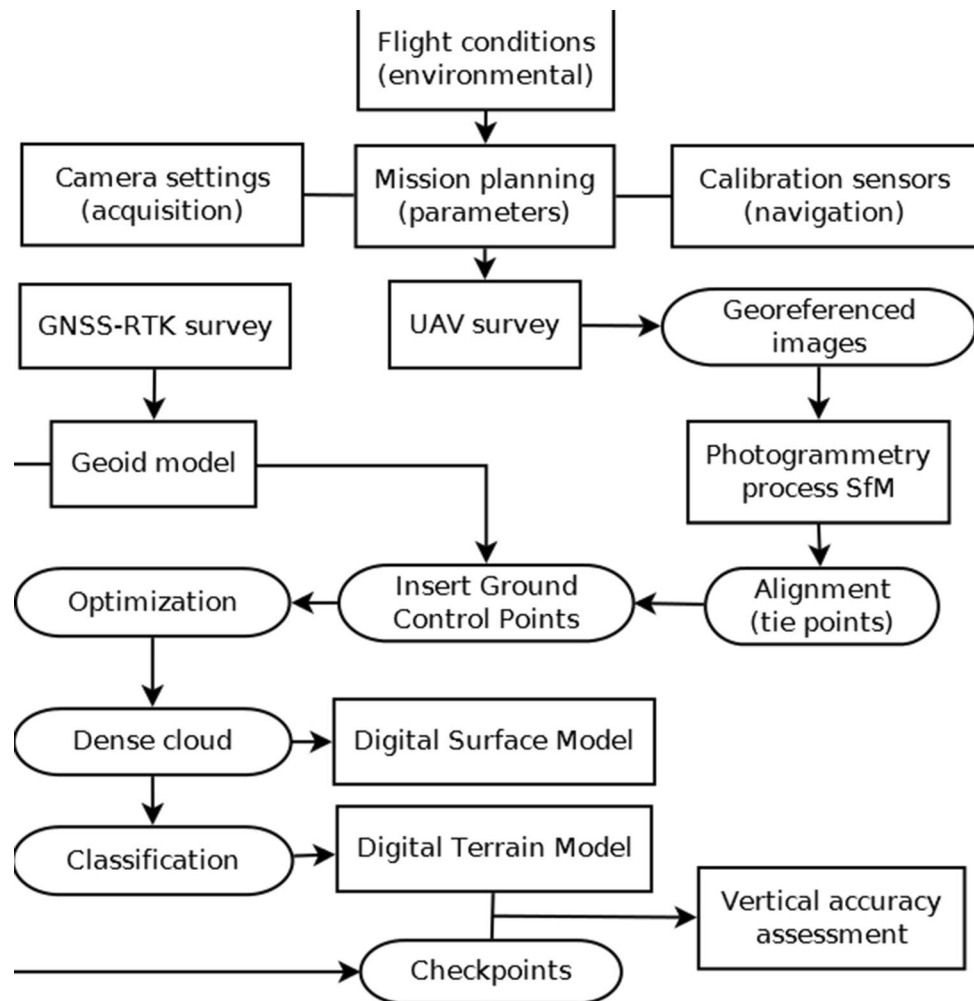
active coastal strip flight plans (foredune ridges and shore) executed on a single survey day in September 2018. The completion of each flight plan took an average of 18 min, depending on wind conditions (direction and intensity), always respecting the 19.5 kt limit for safe operation [50]. The UAV flight plan settings are summarized in Table 1.

In parallel to the flight preparations, the photogrammetric targets were distributed or human-made features occupied along the area that would be immediately over-flight, and the coordinates' acquisition by real-time kinematic positioning (RTK) is performed in Fig. 2. Ground control point (GCP) and check point (CKP) surveys were performed using the Leica GS15 GNSS receiver (L1, L2, L2C signals) and Pacific Crest T300 external radio operating in the geodetic mode (PDOP < 4) with RTK positioning acquisition. The base antenna was stationed over on a survey control with coordinates relative to the Brazilian Geodetic System (SGB) network, as shown in Fig. 2a. The targets were occupied for 5 min (semikinematic or stop-and-go) with the rover antenna using a tripod for stabilization, as shown in Fig. 2b and c. The GNSS-RTK survey

accounted for 68 GCPs for use in bundle block adjustment and 42 CKPs for the digital terrain model (DTM) validation. Also, coordinates were collected in the streams that in the captured images presented obstructions to hydrological connectivity, such as small bridges and road culverts, as shown in Fig. 2d supporting the hydro-enforcement step. All ellipsoidal height coordinates obtained by the surveys were adjusted to orthometric heights through the geoid heights provided by MAPGEO2015 software, available from the Instituto Brasileiro de Geografia e Estatística (IBGE).

2.3 UAV-SfM processing

The images in the JPEG format were processed in Pix4D mapper, a photogrammetric application that uses the structure-from-motion (SfM) algorithm. According to Turner et al. [13], SfM is a computational technique developed in the 1990s and popularized in the last ten years within the digital photogrammetry field. SfM is used to reconstruct objects or scenes from a series of high

overlapping photographs obtained in different positions and orientations due to variation in the acquisition perspective [10, 14]. SfM can recognize patterns and textures, estimate target position, and calculate block geometry using computer vision algorithms [16]. Also, according to Turner et al. [13], the SfM application in surveys for topographic purposes consists in the automated detection and processing of homologous points present in the surface image set (2D), obtaining a high-density three-dimensional point cloud (3D), the primary input for the construction of DEMs and orthomosaics, for example.

Before processing, all the information about the aircraft geolocation and the images georeferencing (geotagging via GPS and on-board barometer) were checked by DJI Assistant and GeoSetter software. The UAV/GNSS-RTK data acquisition hierarchy, processing, and verification steps can be viewed with the help of the workflow, as shown in Fig. 3. For data processing, a high-performance workstation was employed. Fine spatial resolution surface modeling requires high computational performance. Even with the popularization and consequent cheapness of UAVs, the computational cost of image processing for photogrammetric purposes still requires significant hardware investment. The processing time for the 3155 images block was approximately 30 h, not including in the sum: the insertion steps of GCPs and the densified point cloud classification for the DTM generation.

The initial step into the Pix4D was to pre-align the images in a spatial reference system, where the surface was first reconstructed and rendered as a sparse X, Y, Z coordinate point cloud. The algorithm extracted and identified tie points presented in distinct images, creating a series of links, followed by optimization that calibrated the model from the camera's internal (obtained from the EXIF metadata) and external parameters [14, 16]. After the alignment and obtaining the sparse points cloud, the GCPs were inserted, and the re-optimization was performed, thus introducing the three-dimensional coordinates from the GNSS-RTK survey, which minimized

bundle block distortions and provided the highest design precision.

The workflow steps consisted of the following products creation: the dense point cloud, generating more link points between images for increased data redundancy (median of 54,467 keypoints per image); the digital surface model (DSM), through the interpolation of the point grid densified by the inverse distance weighting (IDW) method; and the true orthomosaic formed in RGB composition by the set of adequately orthorectified images. The last UAV-SfM step in the Pix4D software comprised the dense point cloud classification through an automated routine according to the corresponding surface/target from a sample selection, typifying it as: ground (dunes and undergrowths), road surface (shore/beach, dune flat areas and roads), vegetation (shrubbery), buildings, and human-made object (such as walls, utility pole and vehicles). Ground and road surface features were also interpolated by the IDW method. Other generated products composed the project, such as the textured 3D mesh and contour lines, which is not covered in detail here, as they were not employed in the bathtub modeling.

2.4 Coastline benchmark determination

The elevation is the most important feature in assessing coastal flooding through geospatial modeling [18, 51, 52], and it is necessary to correlate the altimetric accuracy obtained in the topographic data collection with a local reference level [1]. The definition and detection of a practical reference for the physical land–water boundary are controversial, employing different terminologies and methods according to the chosen indicator feature and data availability [53]. Coastal flooding modeling usually adopts a vertical datum based on a tidal series or tidal datum [17, 19]. The tidal reference records the amplitude of the oscillations, and maximum values are usually used as the starting level modeling [6, 17, 18]. However, the

Fig. 4 Scheme with the terminology and reference employed for the coastline Adapted from [76].
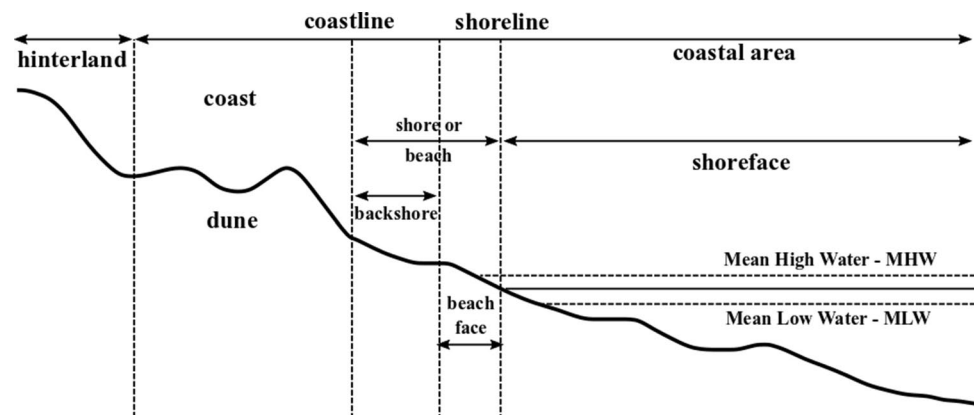
historical tide series are not always available. Inconsistency in a series, multiplicity of local date, or even absence of a nearby station could make it impossible to adopt a tidal datum [16, 18, 51, 52].

In the case of the study area, the nearest tidal station is located within a lagoon system, being controlled by different forces of the beach shoreline variation, and its use as a proxy is not possible [40]. In the absence of tidal data or datum mismatch, the bibliography presents other techniques for settle a vertical reference, such as recording waterline position or morphology through topographic profiles; GNSS-RTK survey and LiDAR; the average position of the waterline through video–image orthorectification; stretch limit segmentation, erosive escarpment, dune crest/base or dry/wet sand tone detection in aerial photographs and satellite sensor images. Further information on such approaches can be found in Boak and Turner [53, 54], Stockdon et al. [55], Pereira et al. [56]; Santos et al. [57], Goulart and Calliari [58], Muehe and Klumb-Oliveira [59]. The high-resolution topographic data availability enables the particularization of the coastal micro-relief [60], as shown by Stockdon et al. [55] by applying foredune ridge identification algorithms with LiDAR data for use in coastal flooding models.

We used a multi-criteria set for the detection and geomorphometry delimitation of the foredune ridges base or 'front dune foot,' as shown in Fig. 4. In the study area, the base of the foredune ridges is the first prominent feature of the subaerial profile, the topography break between the beach system (a real ramp for the action of the waves, wide and with low slope) and the dune system [40, 44]. Such feature is considered more stable and suitable for the coastline delimitation, corresponding to the interface between the upper limit of the backshore with the dune system in sandy beaches [61], commonly delimited by high-resolution aerial photographs [53, 54, 62]. In this sense, the determination of the coastline by geomorphometry criteria is more reliable than the usual two-dimensional image analysis. The UAV survey on the foredune ridges and beach was carried out entirely in the erosive seasons of the profile, which for modeling purposes represents the mean reach of marine action toward the hinterland.

The benchmark determination step initially consisted of the UAS-SfM DTM derivation in two new surface rasters, slope and aspect, which made up the inputs of the multicriteria expression. The slope can be defined as the angle of the local surface inclination in relation to the horizontal plane, determining the flow velocity by gravity [63]. For Li et al. [64], the slope is a DEM primary derivation, because it expresses, besides the gradient itself, the slope direction called aspect. The aspect is the horizontal angle of the surface flow direction driven by gravity, being measured clockwise and generally expressed in the azimuthal form according to the geographic North [63]. The condition intervals were extracted through 200 cross-shore transects distributed equidistantly (25 m) along the 5 km of the coastal strip. Therefore, we determined the occurrence range of the backshore-dune system transition identifying the geomorphologic natural break. With the delimitation of the transition (coastline feature) occurrence range, the elevation value for the DTM was extracted. Thus, the inundation modeling benchmark refers, assumed here as the "vertical zero" of the inundation model, to the mean elevation value of the coastline feature.

2.5 Hydrologic enforcement and DTM accuracy assessment

The altimetric surveys performed by imaging sensors or laser scanning coupled to aerial platforms have as their first return surface, the soil itself and any objects on it, constituting a DSM [65]. The extensive sample coverage provided by aerial platforms coupled with very high-resolution sensors tends to generate very detailed DSMs, creating a series of artificial obstacles that prevent flow connectivity in hydrological models [4, 66], even with the point

Fig. 5 Example of applying the mosaicking technique for hydro-enforcement. **a** Before processing, the road culvert surface blocks the water flow. **b** After processing, the opening simulates the water passage allowed by the culvert
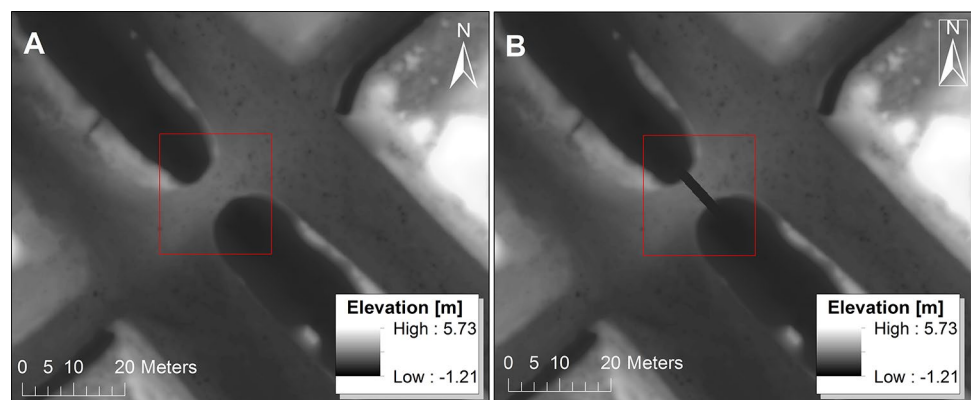
cloud classification for DTM derivation. In this sense, for the reliable representation of the floodplain and eventual drainage lines in coastal areas, it is necessary to correct the digital surface, removing obstacles and checking the naturalness of the water flow by streams that have bridges or culverts along their extension, for example [2, 4, 66].

According to Schimid et al. [19] and Poppenga and Worstell [66], paludal environments and low-lying coastal areas are more susceptible to inaccuracy promoted by DSM registers, because the few protruding features could result in increases in the elevation values, in contrast to the low topographic amplitude naturally associated with these landscapes. For Yunus et al. [6], this increase in elevation inherent in DSMs results in smaller extensions in flood estimates and maybe a source of underestimation in the affected area. Additionally, Poppenga and Worstell [66] point out that obstructions in the hydrological flow decisively impact the quality of the surface modeling flood assessment, as it interferes with the rules of displacement between cells/pixels, disfiguring the environment's real connectivity.

Connectivity correction techniques are known as hydro-enforcement, and the expected result is the approximation of the digital surface to its natural hydrological characteristics, thus reducing the uncertainties associated with a false blockage in water flow [4, 66]. For this work, the recommendations proposed by Yunus et al. [6] and Poppenga and Worstell [66] through the use of hybrid DTM,

with airborne sensor surveys, added to ground surveys were followed. The execution resembles GCP surveys but with a posteriori insertion. The GNSS-RTK acquisitions have been made in streams that naturally allow ocean waters to invade the hinterland in storm surges episodes, but have bridges or road culverts. The data were interpolated by the IDW method and delimited according to the corresponding stream margins, with the resulting raster overlapping to the DTM through mosaicking, as shown in Fig. 5. With the hydro-enforcement step finished, thus obtaining the definitive fine-resolution DTM, the root-mean-square-error (RMSE) accuracy assessment, the spatial distribution of the discrepancy values, and standard deviation were performed.

2.6 Application of the bathtub model using GIS software

The bathtub model is a recurrent methodological approach for use in coastal flood and inundation assessments [2, 5, 6, 17, 19]. It is a hydrostatic geospatial proposal that uses DEMs for water simulation, with a structure strongly dependent on the topographic input data quality [2, 5, 6, 19]. Its name refers to the 'bathtub fill' process [67], generating information on the extent and depth of flooding as water flow fills the morphometric areas of interest and can be implemented via GIS [6, 66], which facilitates

Fig. 6 Workflow of bathtub approach in GIS software Adapted from [31]
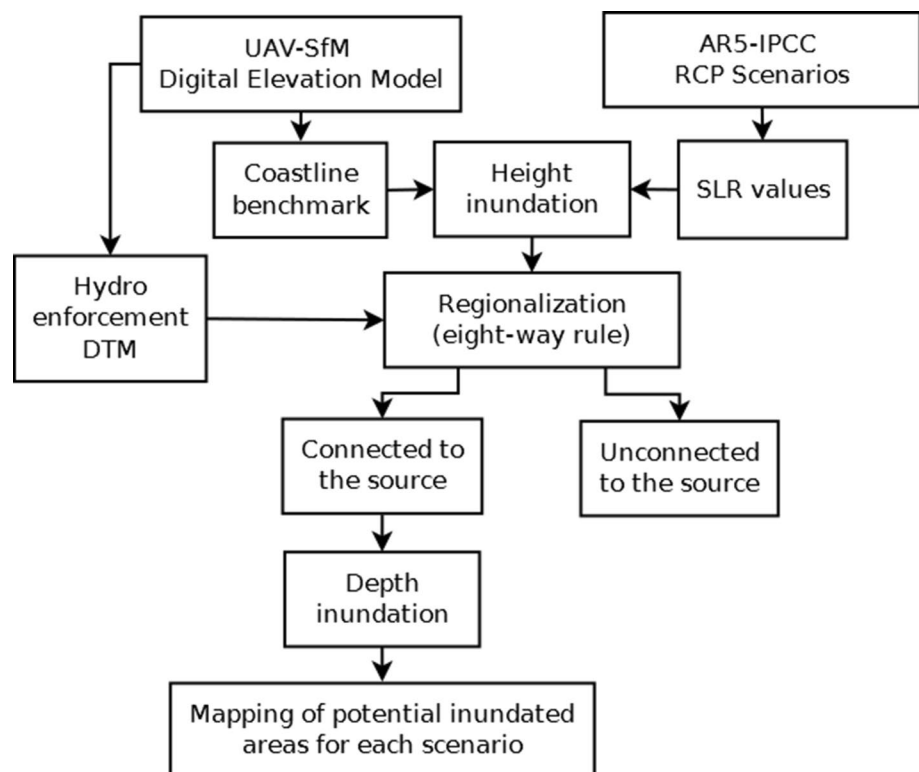
integration with other georeferenced information plans [5].

For the sea-level rise scenarios simulation, the modified bathtub model was applied according to the National Oceanic and Atmospheric Administration Office for Coastal Management [31] for use in the coastal inundation mapping. The method consists of the information plans hierarchical processing executed through tools present in ESRI's ArcGIS 10 software, facilitating the information integration, statistical derivation, and cartographic composition. The methodological steps of the modified bathtub approach can be viewed in the workflow, as shown in Fig. 6.

As described above, instead of a maximum tidal datum (as the usually applied mean high water—MHW or mean higher high water—MHHW), a morphological feature was adopted as a benchmark for the current conditions surface: the mean elevation value of the foredune ridges base, taken as the study area coastline, was extracted from the DTM using morphometric criteria (slope and aspect). The projected SLR values were taken from the 5th Intergovernmental Panel on Climate Change or AR5-IPCC report [20]. In total, 36 SLR values were simulated, covering the four representative concentration pathway (RCP) scenarios proposed by the AR5-IPCC in the 2046–2065

ranges (0.17–0.38 m), 2081–2100 (0.26–0.82 m) and 2100 (0.28–0.98 m).

The simulation assumes that the water body will advance overall topographic elevations at or below the projected water level as long as there is a direct connection to the water source or inundated neighboring cells [6, 17, 67]. Each of the simulations starts from the current coastline plus the predicted SLR value through addition by map algebra (raster calculator tool). In the expression, it is defined that DTM elevation with height values lower or equal to the SLR projection will be drowned. After obtaining the raster surface representing the area affected by the SLR, the next step allows the inundated areas regionalization, according to the topological criteria of hydroconnectivity. According to Poulter and Halpin [2] and Yunus et al. [6], the bathtub approach application resides fundamentally in the adjacent displacement of the surface hydrological flow, a condition associated with data spatial resolution and topological connectivity rules.

An offset rule between cells/pixels is selected according to a possible movement pattern. The zero-side type is applied in the pure conception of the bathtub, where there is no displacement, that is, the single condition rule states that the cell is flooded instantly if its elevation is equal to or less than the projected dimension. The four-side and eight-side rules establish paths connecting the adjacent cells that go back to the flood source. According to Poulter and Halpin [68], the four-side (D4) uses connections between cells located in the cardinal positions, while the eight-side rule (D8) adds to these four diagonal positions, promoting the evaluation of eight possible ways, rule adopted in the present study. In the eight-side rule, the eight neighboring pixels are inspected to determine the hydrological flow, and it is also possible to determine the areas susceptible topographically but not flooded due to the disconnection with the ocean source [2, 6]. Determining the inundation surface according to cell connectivity makes it feasible to identify the depth of each pixel/cell reached, as well as derived information about the drowned area from the SLR.

Table 2 Statistical summary of photogrammetric block processing parameters

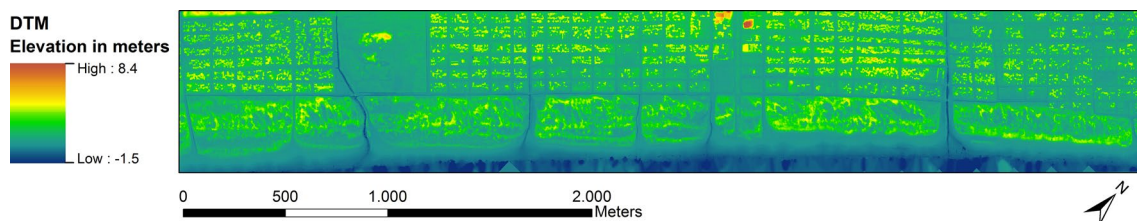| Parameter	Value/rating
Area covered	424.81 ha
Geolocated images	3155/3155
Calibrated images	3096/3155
Overlap density	> 5 images
Matching per image	15,606.1
Georeferencing	68 GCPs
Dense cloud	$> 476 \times 10^6$
Bundle adjustment RMSE [3D]	0.052 m
Projection error [pixels]	0.469
Horizontal accuracy RMSE [east/north]	0.040/0.049 m
DSM and orthomosaic [GSD]	0.0259 m

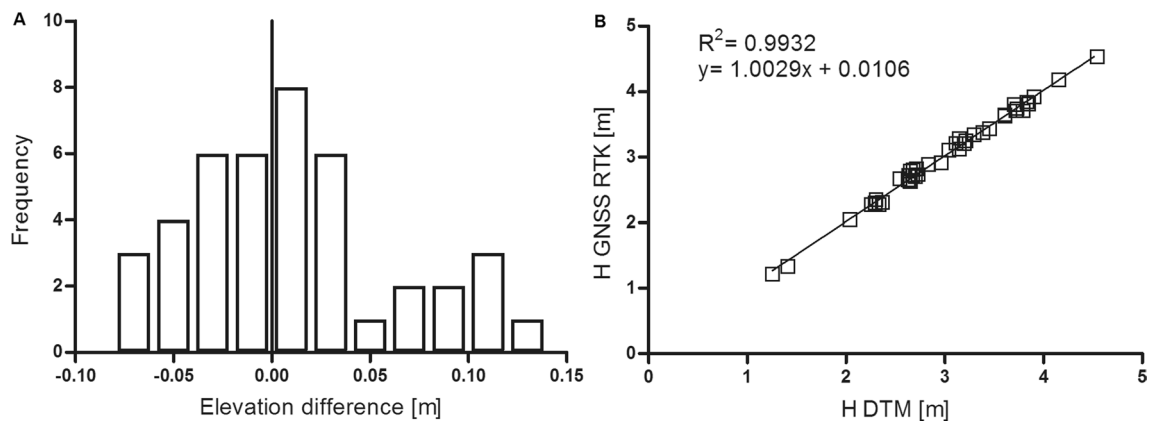**Fig. 7** Digital terrain model of Cassino Beach using UAV-SfM techniques

Fig. 8 a Frequency and distribution of elevation errors; **b** coefficient of determination (R^2) for elevation between independent check points (CKPs) and DTM

3 Results and discussion

3.1 UAV-SfM-based high-resolution coastal DEM

The UAV survey resulted in 3155 images, of these 3096 were calibrated correctly (about 98%) in the process of alignment and topographic reconstruction of the area of interest. The 59 uncalibrated correspond to the images obtained over the shoreline. According to Turner et al. [13], extremely dynamic features such as the swash zone limit the identification of matching points, because there is no point acquisition for non-stationary features, essential to the processing for the SfM algorithm. This limitation did not affect the following step of the methodology, since the bathtub model had the coastline as a benchmark, disregarding the beach face. The 80% (front) by 60% (side) overlap setting gave an image overlap density higher than five images for most of the study area, with the predictable exception for the boundary and the swash zone. Each calibrated image obtained a median of 15,606.1 matches, guaranteeing a reliable reconstruction even of small morphologies.

The internal bundle block adjustment was performed through 68 GCPs obtained by GNSS-RTK, resulting in a root mean square error (RMSE) of 0.052 m. The projection error was sub-pixel, with a mean of 0.469. Both results demonstrate the quality of the images obtained since the targets were adequately identified and georeferenced. Each GCP was identified on average by seven images, totaling 476 photographs where targets were identified (placing markers), excluding targets that were not entirely in the photograph or those that had a blur effect (< 1% of the total images). The dense cloud obtained by the project consists of more than 476×10^6 points, with an average density of 170.4 points/m^3. Products derived from dense cloud (DSM

and orthomosaic) resulted in a ground sample distance (GSD) of 0.0259 m, highlighting the high resolution of the image output, precisely at the GSD calculated during the flight planning step. The statistics of the bundle adjustment processing are summarized in Table 2.

After the dense cloud classification, keeping only the surfaces that correspond to the ground, and the execution of the hydro-enforcement step, the DTM resulted in a very-high-resolution raster with a GSD of 0.1294 cm/pixel, as shown in Fig. 7. The loss of spatial resolution between DSM, the primary raster output, and DTM is due to a decrease in the point cloud used after classification. The evaluation of the DTM vertical accuracy employing 42 independent checkpoints (CKPs) resulted in an RMSE of 0.0607 m. Similar values were found by Ulysal et al. [69], Gonçalves and Henriques [8], Woodget et al. [70], Chen et al. [71], Elsner et al. [15], and Ravanelli et al. [72] using UAV-SfM techniques, although with different flight parameters and cover areas. The standard deviation was 0.0582 m, but the street CKPs' standard deviation within the urban area was higher (0.0543 m) than those positioned on the dunes and backshore (0.0384 m). The most significant discrepancies were identified at the boundary of the DTM and in the consolidated urban area (e.g., where trees and buildings were present).

According to Gonçalves and Henriques [8] and Gašparović et al. [73], the residual error distribution in UAV-SfM-based DEMs does not usually follow a normal distribution due to possible systematic measurement errors. This is also demonstrated in the work of Mancini et al. [10]. Even with the most appropriate camera calibration and use of a tripod for GNSS-RTK acquisition, errors associated with shadows projection on the streets add to the errors inherent in urban surveys (multi-path signal, for example), which are the most likely sources of discrepancies, as

Fig. 9 Bathtub modeling for the 2046–2065 range of IPCC sea-level rise projections for Cassino Beach

shown in Fig. 8a). Errors associated with changes in lighting in different blocks (different survey days), with distinct cloud cover and solar angle as pointed out by Nex and Remondino [16], are also not ruled out. In this sense, the targets positioned over dunes and wide streets obtained the lowest error values, increasing the average accuracy of the model. Despite these limitations, the coefficient of determination between CKPs and DTM showed a robust linear adjustment to the vertical coordinate, as shown in Fig. 8b). According to Mendez-Barroso et al. [11], the most significant residual errors in boundary areas are common in the SfM-derived DEMs and can be minimized by widening the area of interest or distributing more GCPs at the edges. To overcome this problem, in the present work, the boundaries of the DTM were discarded, reducing the area of interest compared to the UAV survey area.

The results demonstrate the importance of using GCPs to increase the accuracy of the bundle adjustment. The concern with this inaccuracy is justified, because according to Poulter and Halpin [2] in many cases the vertical error may exceed the increment values promoted by projections and sea-level rise scenarios. Although the amount and form of distribution of GCPs are still widely debated, depending heavily on the topography and extent of the

area of interest, their use is essential in reconstructing high-resolution DEMs [9, 16]. However, it is noteworthy that no checks were performed on streams with water depths greater than 0.50 m—deeper portion of the washouts. According to Turner et al. [13], deep water surfaces may be erroneously allocated in the outliers due to the spectral characteristics of water absorption and reflection. Submerged error behavior information for UAV data due to light refraction/absorption at the air–water interface can be found in Woodget et al. [70].

3.2 Inundation mapping for sea-level rise scenarios with bathtub approach

For this study, the bathtub model was applied to simulate 36 projections of sea-level rise proposed by the IPCC [20], following the modified approach by NOAA [31]. The projections are divided into 20-year intervals and an end of century according to each representative concentration pathway (RCP) scenarios. The result of climate modeling is an optimistic scenario (RCP2.6), two intermediate stabilization (RCP4.5 and RCP6.0), and one pessimistic (RCP8.5) scenario. Each scenario presents different responses according to the energy storage of the terrestrial system.
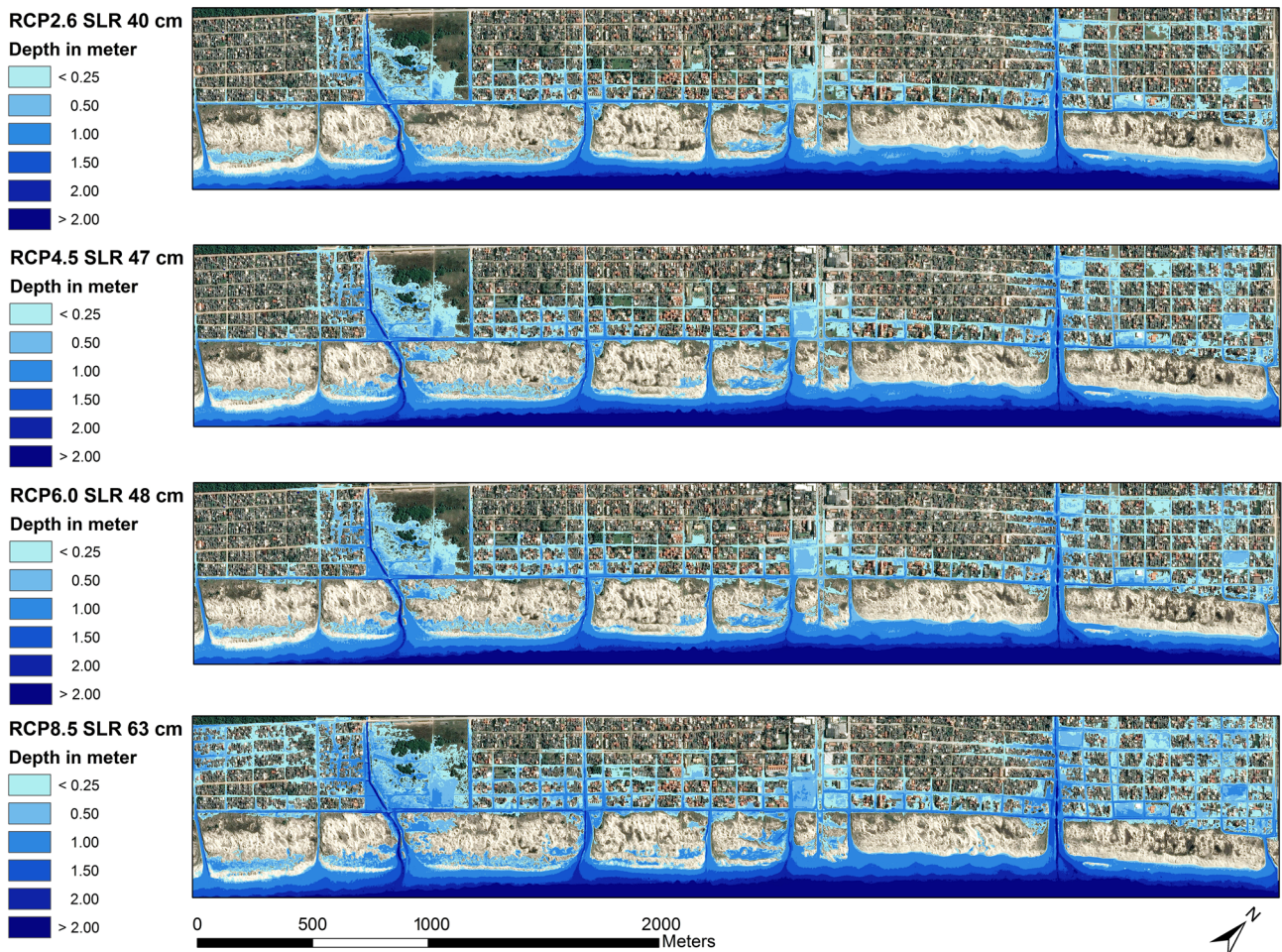
Fig. 10 Bathtub modeling for the 2081–2100 range of IPCC sea-level rise projections for Cassino Beach

The projections have ranges according to the parameters variance, with minimum, median, and maximum values. All these values were applied to Cassino beach. The median intervals of each scenario, sea-level rise values with likely ranges between 66 and 100% [20], are expressed in the following maps, as shown in Figs. 9, 10, and 11. Table 3 shows the exposed area in hectares for all the projections, as well as the percentage of inundation area based on the totality of the DTM (total model area) and only for the urban area (discarding the dunefield area).

The projections for the first interval, Fig. 9, show the high topographic susceptibility of the Cassino Beach, even with the smallest sea-level rise values—between 24 and 30 cm of increase. The extent of drowned areas ranges from 25 to 28% for the entire model and from 37 to 41% for the urban area only. The results show that the streets just at landward from the dune ridge were almost entirely flooded, registering average depths between 0.42 (scenario RCP2.6) and 0.47 m (scenario RCP8.5). The flow pathway is clearly identified as the washouts and man-made

car access to the beach, which allows marine intrusion to reach almost 650 m from the coastline. For the remaining part of the dune, the flooding levels were not sufficient to transpose the dune crest. Important to note that the distal displacement in the streams was only possible due to the hydro-enforcement process since there are road culverts. Poppenga and Worstell [66] point out that the lack of hydrological connectivity in DEM may lead to the exclusion of potentially flood-prone inland areas, which is critical in assessments associated with coastal dynamics.

The car accesses and the drainage streams facilitate marine intrusion into the hinterland as it already happens in episodes of storm surges. These morphologies with the highest inundation potential for the 2046–2065 range are already affected by storm surges. According to Serpa et al. [28], the occurrence of washouts increases the susceptibility of the coastal plain to flood caused by storm surges, which is also true for SLR inundation. Goulart [40] states that the large-amplitude episodes (2 m above the shoreline established for the study) constituted 8% of the
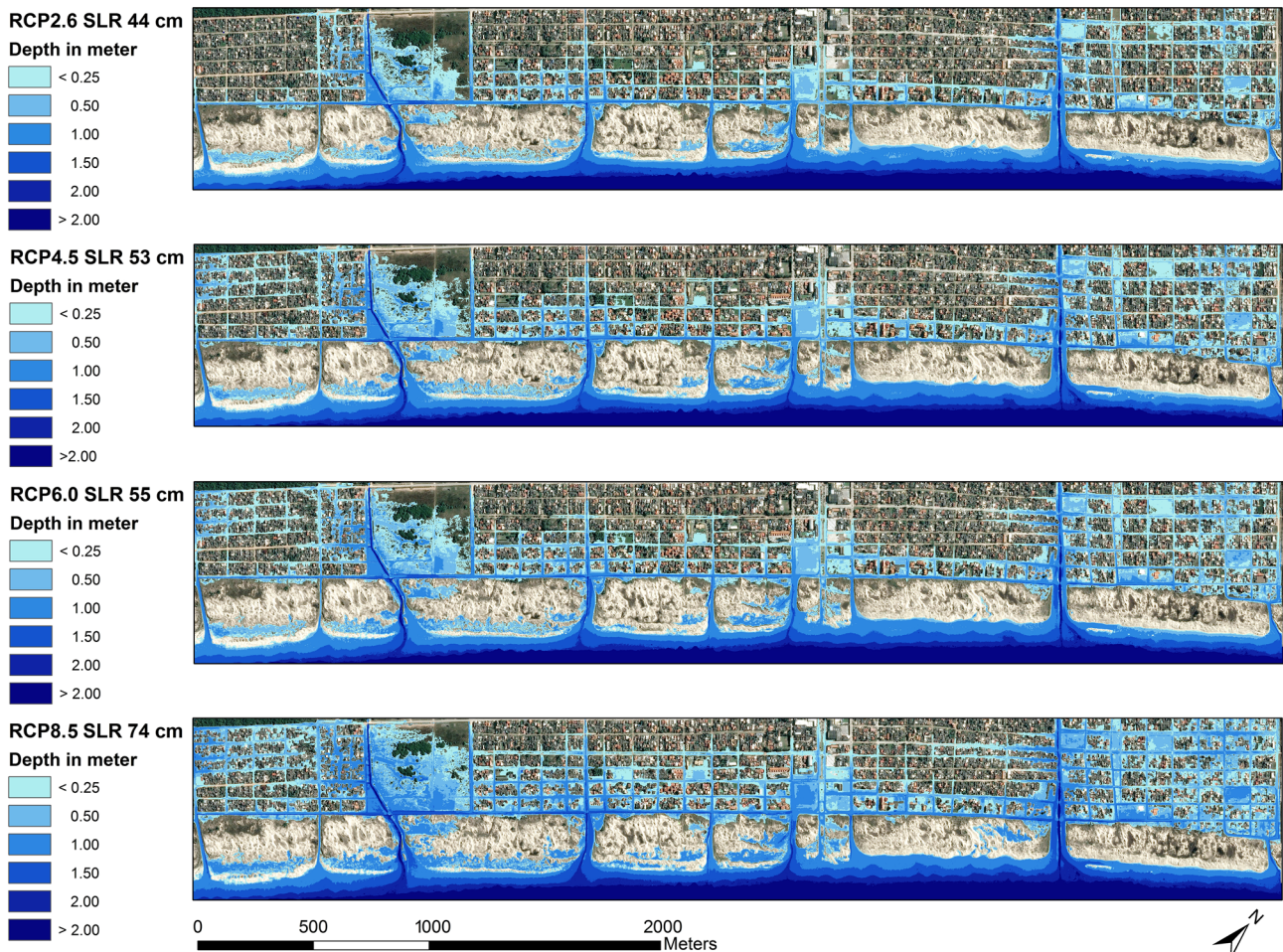
Fig. 11 Bathtub modeling for the 2100 of IPCC sea-level rise projections for Cassino Beach

observations between 2006 and 2010 at Cassino Beach, occurring mainly in the winter months. In these episodes, streets, adjacent houses, and the foredune ridges were impacted. Storm surge events are routine between July, August, and September in the study area due to Atlantic cyclogenesis and are also responsible for major erosive episodes [38, 42, 43].

In a similar time interval, relative sea-level rise projections for the coast of Brazil were prepared by the Economic Commission for Latin America and the Caribbean—ECLAC [74], integrating into the modeling geological and oceanographic characteristics of the region. In it, the SLR projection for Cassino Beach's surroundings reaches 0.27 m by 2040, a rate of approximately 2.21 mm/year. This level is very close to the IPCC projection for the 2046–2065 range and is an intermediate value between the RCP6.0 (stable) and RCP8.5 (pessimistic) scenarios. The regional SLR projection proposed by ECLAC is smaller than the most recent

NASA [75] global average sea level trend, with an increase rate of 3.3 mm/year.

For the last two decades of this century, the SLR varies between 40 and 63 cm, as shown in Fig. 10. The scenarios expand urban areas impacted by inundation: between 34 and 49% for the optimistic and pessimistic scenarios, respectively, and between 51 and 73% only for the urban area. Washouts remain the main flooding pathway of flooding for this coastal area. The projection with higher levels directly impacts the low topography of the floodplains of these drainage streams. In this interval, the water intrusion averages 407 m on the hinterland. However, with the exception of the RCP8.5 scenario, the other three scenarios show a significant expansion of drowned areas but with a low water level (≤ 0.50 m).

In the range 2081–2100, it is possible to identify which topographic depressions of the drainage streams are entirely drowned. Secondarily, the roads and streets of the beach become accessible for intrusion, displacing

Table 3 Sea-level rise modeling for IPCC projections according to time interval and RCP scenario

RCP scenarios	SLR (m)	Exposed area (ha)	Modeling area%[a]	Urban area%[b]	Water depth (m)[c]
IPCC sea-level rise in 2046–2065					
2.6					
Lower	0.17	69.65	22	33	0.01 to 2.25
Median	0.24	77.61	25	37	0.01 to 2.32
Higher	0.32	92.41	29	43	0.01 to 2.40
4.5					
Lower	0.19	71.80	23	34	0.01 to 2.27
Median	0.26	80.64	26	38	0.01 to 2.34
Higher	0.33	94.04	30	44	0.01 to 2.41
6.0					
Lower	0.18	70.80	23	33	0.01 to 2.26
Median	0.25	79.11	25	37	0.01 to 2.33
Higher	0.32	92.41	29	43	0.01 to 2.40
8.5					
Lower	0.22	74.89	24	35	0.01 to 2.31
Median	0.30	86.87	28	41	0.01 to 2.39
Higher	0.38	103.60	33	49	0.01 to 2.47
IPCC sea-level rise in 2081–2100					
2.6					
Lower	0.26	80.64	26	38	0.01 to 2.34
Median	0.40	107.50	34	51	0.01 to 2.48
Higher	0.55	139.20	44	66	0.01 to 2.63
4.5					
Lower	0.32	92.41	29	43	0.01 to 2.40
Median	0.47	120.89	38	57	0.01 to 2.55
Higher	0.63	155.15	49	73	0.01 to 2.71
6.0					
Lower	0.33	94.04	30	44	0.01 to 2.41
Median	0.48	122.63	39	58	0.01 to 2.56
Higher	0.63	155.15	49	73	0.01 to 2.71
8.5					
Lower	0.45	117.50	37	55	0.01 to 2.53
Median	0.63	155.15	49	73	0.01 to 2.71
Higher	0.82	188.73	60	89	0.01 to 2.90
IPCC sea-level rise in 2100					
2.6					
Lower	0.28	84.06	27	40	0.01 to 2.36
Median	0.44	115.78	37	54	0.01 to 2.52
Higher	0.61	151.48	48	71	0.01 to 2.69
4.5					
Lower	0.36	99.42	32	47	0.01 to 2.44
Median	0.53	135.17	43	64	0.01 to 2.61
Higher	0.71	170.23	54	80	0.01 to 2.79
6.0					
Lower	0.38	103.60	33	49	0.01 to 2.47
Median	0.55	139.20	44	66	0.01 to 2.63
Higher	0.73	173.39	55	82	0.01 to 2.81
8.5					
Lower	0.52	131.80	42	62	0.01 to 2.60
Median	0.74	173.72	55	82	0.01 to 2.82
Higher	0.98	210.84	67	99	0.01 to 3.06

[a]Total drowned modeling area;

[b]Urban drowned area (disregarding the dunefield)

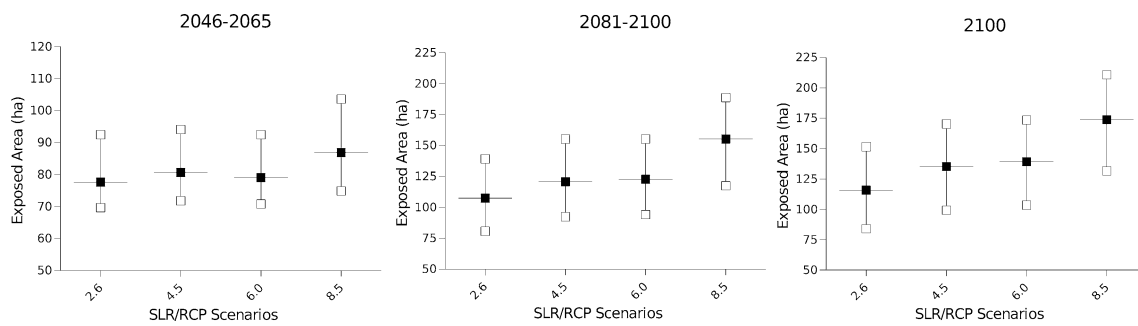[c]Includes depth of drainage streams and shore

Fig. 12 Graph showing the evolution of the exposed area to each RCP scenario in the range 2046–2065, 2081–2100, and 2100. The graphs show the 'higher' and 'lower' values of the impacted area according to the respective scenario, as well as the 'median' values (black squares) expressed in the maps of Figs. 8, 9, and 10

marine water not only distally (as in the previous interval), but also longitudinally. Both processes could be mapped due to the high resolution of the DTM in association with connectivity rules. In this scenario, it also reaches a new flood limit, expanding the cuddled area to the NW portion of the study area, which has expanded to 73% of the drowned urban area. In this interval, it is also evident the swale drowning established to the windward of the foredunes first crest, sectioning them. These areas are likely to be the first to erode during the gradual establishment of SLR of this magnitude, something that bathtub modeling does not predict.

Toward the end of the century, the projections accentuate the water height, with sea-level increase reaching 74 cm, as shown in Fig. 11. More than half of the model area is drowned (55%), and the impact on the urban area exceeds 3/4 (83%). Low washout topographies are still the most impacted in scenarios RCP2.6, but in other scenarios, the connectivity provided by the streets ensures the expansion of drowned areas. The low topography of the SW areas, only drowned in the RCP8.5 scenario of the previous range, is achieved even in the intermediate scenarios. The areas located in NW and SW of the study area have a complex topography associated with aeolian geomorphologies called transgressive dune sheets or TDS [33]. The urban area of the Cassino balneary, Querência, and ABC has expanded over the TDS, overlapping the dune swales. The low topography of these features is more susceptible to flooding during periods of higher rainfall [47], as they are drainage lines that favor water retention in the form of wetlands. When hit by the SLR, connectivity tends to drown these depressions.

In Fig. 12, it is possible to follow the graphical evolution of the exposed area in each interval. In the first interval (2046–2065), the low amplitude of projections (< 40 cm) has a more significant effect on the topography of drainage streams and adjacent streets. The second interval (2081–2100) breaks the previous topographic threshold, with peaks of expansion of the exposed area by exceeding the 40-cm increment of SLR. In it, the optimistic scenario (RCP4.5) finds new connections to the NW area, which are progressively drowned in the intermediate scenarios. A new topographic threshold break is reached from the 63-cm increment in the pessimistic scenario (RCP8.5), which reaches the SW portion. By the end of the twenty-first century, all scenarios exceed the 40-cm threshold, reaching much of the urban area. According to Poulter and Halpin [2], the expansion of the areas affected by the SLR through the bathtub approach is not linear, but abrupt. Upon reaching the most susceptible topographic thresholds, a dike 'breach' event occurs when a portion of the DEM previously inaccessible to the water is abruptly connected to a neighboring flooded cell [2].

Determining the most susceptible topography and threshold areas can assist in mitigating the effects of not only medium- and long-term sea-level rise, but also short-term storm-related fluctuations. According to Martínez-Graña et al. [51], coastal areas with a low slope have a high potential for seawater displacement toward the hinterland, also controlling withdrawal velocity after extreme events. In the same vein, Paprotny and Terefenko [67] point out that long-lasting storms can flood even larger areas and reach higher topographies in gently sloping environments, especially on exposed coasts. Low-lying coasts with morphology associated with depositional systems (such as barrier-lagoon) present great difficulty in draining excess water, usually presenting secondary scenarios of flooding by damming of marine water, even after days of the storm surge event. Importantly, this is not only due to morphological factors, such as the inefficiency of ephemeral streams [52], but also due to the dynamics of the water table [67]. All the factors listed are part of the study area configuration, increasing the need to address the potential effects of SLR inundation or storm surge flooding—such as

planning urban sprawl, conserving foredune ridges, and managing drainage systems, especially washouts.

4 Conclusions

The results demonstrated the accuracy of the UAV-SfM-derived DTM, with RMSE of 0.0607 m, close to those found in studies that applied similar methodology and considerably lower than the SLR levels of the projections, confirming that the proper configuration of the aircraft and its sensors, coupled with rigorous ground control through the GNSS-RTK receiver, results in topographic surfaces with centimeter precision. Thus, the implementation of the connectivity rules was decisive for inundation mapping, as it valued the micro-features obtained by the DTM with a resolution of 0.1294 m. The absence of a tide gauge station was circumvented by using data derived from DEM itself, showing a functional alternative based on geodetic values. However, a tide gauge series would provide a robust reference to the standard maximum levels (MHW or MHHW) and the return period of the study area, which would increase the sophistication of the projections.

The 36 projections were carried out according to the fifth IPCC report, which covers a wide range of flood levels reaching different portions of the study area. It was possible to determine a topographic threshold, where SLR effects are most significant. This threshold corresponds to the increase from 0.40 m above the current coastline and will be reached in the last two decades of this century, even in the most optimistic scenario. It is essential to highlight that the areas with the highest flood potential for the 2046–2065 interval are already sporadically affected by storm surges, but with lower water height. In the analysis of SLR scenarios, it was possible to identify that: (1) the coastal streams (washouts) and the access roads to the beach are the preferred inundation paths since none of the projections flooded the foredune ridges; (2) the transgressive dune sheets topography, the geological substrate of the urban area, controls the flooding patterns in the hinterland, with special susceptibility in depressions formed by drainage lines and dune swales.

The bathtub modeling evidenced that low-lying coasts are highly susceptible to SLR effects. Coupled with the permanent inundation caused by climate change, Cassino Beach is vulnerable to the south quadrant winds, which is the source of significant storms. The combined action of storm surges and SLR scenarios can magnify the flooding effects that already occur. Leading to the expansion of floodplains, wetlands, as well as groundwater rise, which can overwhelm sanitation infrastructure. Climate change also indicates changes in precipitation patterns (frequency and intensity), causing severe conditions of composite flooding. Scenarios of this nature will gradually hinder everyday life and may reach a risky condition. It should be noted that the flood simulations of this work have scientific objectives, and their results should not be adopted singly for decision making, especially for infrastructure and economic purposes. The mapping identifies the topographically exposed areas with the highest drowning potential, but does not incorporate sedimentary changes and assumes that current topography will persist throughout the century.

Availability of data and material The rasters data will not be made available because they will be used in other studies.

Compliance with ethical standards

Conflicts of interest The authors declare that they have no conflict of interest.

References

1. Gesch DB (2009) Analysis of Lidar elevation data for improved identification and delineation of lands vulnerable to sea-level rise. J Coast Res SI 53:49–58. https://doi.org/10.2112/SI53-006.1
2. Poulter B, Halpin PN (2008) Raster modelling of coastal flooding from sea-level rise. Int J Geogr Inf Sci 22(2):167–182. https://doi.org/10.1080/13658810701371858
3. Gruber S, Peckham S (2009) Land-surface parameters and objects in Hydrology. In: Hengl T, Reuter HI (eds) Geomorphometry: concepts, software, applications. Elsevier, Holanda, pp 171–194
4. Poppenga SK, Worstell BB, Stoker JM, Greenlee SK (2010) Using selective drainage methods to extract continuous surface flow from 1-meter derived digital elevation data: U. S. Geological Survey Scientific Investigations Report 2010–5059. U. S. Geological Survey Report 12
5. Seenath A, Wilson M, Miller K (2016) Hydrodynamic versus GIS modelling for coastal flood vulnerability assessment: which is better for guiding coastal management? Ocean Coast Manag 120:99–109. https://doi.org/10.1016/j.ocecoaman.2015.11.019
6. Yunus AP, Avtar R, Kraines S, Yamamuro M, Lindberg F, Grimmond CSB (2016) Uncertainties in tidally adjusted estimates of sea level rise flooding (bathtub model) for the greater London. Remote Sens 8(5):1–23
7. Colomina I, Molina P (2014) Unmanned aerial systems for photogrammetry and remote sensing: a review. ISPRS J Photogramm Remote Sens 92:79–97. https://doi.org/10.1016/j.isprsjprs.2014.02.013

8. Gonçalves JA, Henriques R (2015) UAV photogrammetry for topographic monitoring of coastal areas. ISPRS J Photogramm Remote Sens 104:101–111. https://doi.org/10.1016/j.isprs jprs.2015.02.009

9. James MR, Robson S, D'Oleire-Oltmanns S, Niethammer U (2017) Optimising UAV topographic surveys processed with structure-from-motion: ground control quality, quantity and bundle adjustment. Geomorphology 280:51–66

10. Mancini F, Dubbini M, Gattelli M, Stecchi F, Fabbri S, Gabbianelli G (2013) Using unmanned aerial vehicles (UAV) for high-resolution reconstruction of topography: the structure from motion approach on coastal environments. Remote Sens 5(12):6880–6898. https://doi.org/10.3390/rs5126880

11. Méndez-Barroso LA, Zárate-Valdez JL, Robles-Morúa A (2018) Estimation of hydromorphological attributes of a small forested catchment by applying the structure from motion (SfM) approach. Int J Appl Earth Obs Geoinf 69:186–197

12. O'Connor J, Smith MJ, James MR (2017) Cameras and settings for aerial surveys in the geosciences: optimising image data. Prog Phys Geogr 41(3):325–344

13. Turner IL, Harley MD, Drummond CD (2016) UAVs for coastal surveying. Coast Eng (Short Commun) 114(19–24):6

14. Westoby MJ, Brasington J, Glasser NF, Hambrey MJ, Reynolds JM (2012) 'Structure-from-Motion' photogrammetry: a low-cost, effective tool for geoscience applications. Geomorphology 179:300–314

15. Elsner P, Dornbusch U, Thomas I, Amos D, Bovington J, Horn D (2018) Coincident beach surveys using UAS, vehicle mounted and airborne laser scanner: point cloud inter-comparison and effects of surface type heterogeneity on elevation accuracies. Remote Sens Environ 208:15–26

16. Nex F, Remondino F (2014) UAV for 3D mapping applications: a review. Appl Geomat 6(1):1–15

17. Kruel S (2016) The impacts of sea-level rise on tidal flooding in boston massachusetts. J Coast Res 32(6):1302–1309. https://doi.org/10.2112/JCOASTRES-D-15-00100.1

18. Murdukhayeva A, August P, Bradley M, Labash C, Shaw N (2013) Assessment of inundation risk from sea level rise and storm surge in northeastern coastal national parks. J Coast Res 29(6a):1–16. https://doi.org/10.2112/JCOASTRES-D-12-00196.1

19. Schmid K, Hadley B, Waters K (2014) Mapping and portraying inundation uncertainty of bathtub-type models. J Coasta Res 30(3):548–561. https://doi.org/10.2112/JCOASTRES-D-13-00118.1

20. Church JA, Clark PU, Cazenave A, Gregory JM, Jevrejeva S, Levermann A, Merrifield MA, Milne GA, Nerem RS, Nunn PD, Payne AJ, Pfeffer WT, Stammer D, Unnikrishnan AS (2013). Sea level change. In: Climate Change 2013: The Physical Science Basis. Cambridge University Press, Cambridge, United Kingdom and New York, NY, USA

21. Nicholls RJ, Cazenave A (2010) Sea-level rise and its impact on coastal zones. Science 328(5985):1517–1520. https://doi.org/10.1126/science.1185782

22. Tedesco M, Fettweis X (2020) Unprecedented atmospheric conditions (1948–2019) drive the 2019 exceptional melting season over the Greenland ice sheet. Cryosphere 14(4):1209–1223

23. Whitehouse PL, Gomez N, King MA, Wiens DA (2019) Solid Earth change and the evolution of the Antarctic Ice sheet. Nat Commun 10(1):1–14. https://doi.org/10.1038/s41467-018-08068-y

24. Serreze MC, Meier WN (2019) The Arctic's sea ice cover: trends, variability, predictability, and comparisons to the Antarctic. Ann N Y Acad Sci 1436(1):36–53. https://doi.org/10.1111/nyas.13856

25. Wong PP, Losada IJ, Gattuso JP, Hinkel J, Khattabi A, McInnes KL, Saito Y, Sallenger A (2014) Coastal systems and low-lying areas. In: climate change 2014: impacts, adaptation, and vulnerability. Part A: global and sectoral aspects. Contribution of working

group II to the fifth assessment report of the intergovernmental panel on climate change. Cambridge University Press, Cambridge, United Kingdom and New York, 361–409

26. Nicholls RJ, Hanson SE, Lowe JA, Warrick RA, Lu X, Long AJ (2014) Sea-level scenarios for evaluating coastal impacts. WIREs Clim Change 5:129–150. https://doi.org/10.1002/wcc.253

27. Figueiredo SA, Calliari LJ (2005) Sangradouros: distribuição espacial, variação sazonal, padrões morfológicos e implicações no Gerenciamento Costeiro. Gravel 3:47–57

28. Serpa CG, Romeu MAR, Fontoura LAS, Calliari LJ, Melo E, Albuquerque MG (2011) Study of the responsible factors for the closure of an intermittent washout during a storm surge, Rio Grande do Sul, Brazil. J Coast Res SI SI 64:2068–2073

29. Ministério do Meio Ambiente—MMA (2016). Plano nacional de adaptação à mudança do clima. Brasília

30. Painel Brasileiro de Mudanças Climátics—PBMC (2016) Impacto, vulnerabilidade e adaptação das cidades costeiras brasileiras às mudanças climáticas: relatório Especial do Painel Brasileiro de Mudanças Climáticas. PBMC, COPPE-UFRJ. Rio de Janeiro, Brasil, p 184

31. National Oceanic and Atmospheric Administration—NOAA (2017) Detailed method for mapping sea level rise inundation. https://coast.noaa.gov/data/digitalcoast/pdf/slr-inundation-methods.pdf. Accessed 12 Sep 2017

32. Villwock JA, Tomazelli LJ (1995) Geologia costeira do Rio Grande do Sul. CECO/UFRGS, Porto Alegre, p 45

33. Dillenburg SR, Barboza EG, Rosa MLCC, Caron F, Sawakuchi AO (2017) The complex prograded cassino barrier in southern Brazil: Geological and morphological evolution and records of climatic, oceanographic and sea-level changes in the last 7–6 ka. Mar Geol 390(June):106–119. https://doi.org/10.1016/j.margeo.2017.06.007

34. Calliari LJ, Klein AH (1993) Características Morfodinâmicas e Sedimentológicas das Praias Oceânicas Entre Rio Grande e Chuí. RS. Pesquisas Em Geociências 20(1):45. https://doi.org/10.22456/1807-9806.21281

35. Corrêa ICS, Weschenfelder J, Calliari LJ, Toldo EE Jr, Nunes C, Baitell R (2019) Plataforma continental do Rio Grande do Sul. In: Dias MS, Bastos AC, Vital H (eds) Plataforma Continental Brasileira. Programa de Geologia e Geofísica Marinha (PPGM), Rio de Janeiro, pp 73–158

36. Dillenburg SR, Barboza EG, Tomazelli LJ, Hesp PA, Clerot LCP, Ayup-Zouain RN (2009) In: Dillenburg SR, Hesp PH (org.) Geology and geomorphology of holocene coastal barriers of Brazil. Springer, 53–91

37. Almeida LESB, Lima SF, Jr Toldo EE (2006) Estimativa da capacidade de transporte de sedimentos a partir de dados de ondas. In: Muehe D (org.) Erosão e progradação do litoral brasileiro, 446–454

38. Goulart ES, Calliari LJ (2011) Morfodinâmica da zona de arrebentação na Praia do Cassino em eventos de maré meteorológica. Anais do XIII Congresso da Associação Brasileira de Estudos do Quaternário ABEQUA 1:5

39. Guimarães PV, Pereira PS, Calliari LJ, Krusche N (2014) Variabilidade temporal do perfil de dunas na Praia do Cassino ,RS, com auxílio de videomonitoramento Argus. Pesquisas Em Geociências 41(3):217–229. https://doi.org/10.22456/1807-9806.78097

40. Goulart ES (2014) Variabilidade morfodinâmica temporal e eventos de inundação em um sistema praial com múltiplos bancos. PhD Thesis. Universidade Federal do Rio Grande—FURG

41. Machado AA, Calliari LJ (2016) Synoptic systems generators of extreme wind in southern Brazil: atmospheric conditions and consequences in the coastal zone. J Coast Res 75(sp1):1182–1186. https://doi.org/10.2112/si75-237.1

42. Machado AA, Calliari LJ, Melo E, Klein AHF (2010) Historical assessment of extreme coastal sea state conditions in southern

Brazil and their relation to erosion episodes. Pan-Am J Aquat Sci 5(2):105–114

43. Parise CK, Calliari LJ, Krusche N (2009) Extreme storm surges in the south of Brazil: atmospheric conditions and shore erosion. Braz J Oceanogr 57(3):175–188. https://doi.org/10.1590/s1679-87592009000300002

44. Guimarães PV, Pereira PS, Calliari LJ, Ellis JT (2016) Behavior and identification of ephemeral sand dunes at the backshore zone using video images. Anais da Academia Brasileira de Ciências 88(3):1357–1369. https://doi.org/10.1590/0001-3765201620150656

45. Instituto Brasileiro de Geografia e Estatística—IBGE (2019). Projeção dos dados censitários 2010: sinopse por setores. Disponível em: <http://censo2010.ibge.gov.br/>. Accessed 12 Nov 2019

46. Lélis RJF (2003) Variabilidade da linha de costa oceânica adjacente às principais desembocaduras do Rio Grande do Sul IO/FURG. Oceanography Institute of the Universidade Federal do Rio Grande, Rio Grande, p 81

47. Leal Alves, D. C. (2013). Análise da vulnerabilidade nos balneários Querência-Atlântico Sul e Hermenegildo (RS) a partir de indicadores geomorfológicos e antrópicos. Dissertation of the Programa de Pós-Graduação em Geografia—PPGGEO/FURG, 121 p

48. Núcleo de Educação e Monitoramento Ambiental—NEMA (2008) Dunas costeiras: manejo e conservação. NEMA, Rio Grande, p 32

49. Conlin M, Cohn N, Ruggiero P (2018) A quantitative comparison of low-cost structure from motion (SfM) data collection platforms on beaches and dunes. J Coast Res 34(6):1341. https://doi.org/10.2112/jcoastres-d-17-00160.1

50. DJI. (2016). Phantom 4 manual. https://www.dji.com/uk/phantom-4

51. Martínez-Graña A, Boskib T, Goya JL, Zazoc C, Dabrio CJ (2016) Coastal-flood risk management in central Algarve: vulnerability and flood risk indices (South Portugal). Ecol Ind 71:302–316. https://doi.org/10.1016/j.ecolind.2016.07.021

52. Wdowinski S, Bray R, Kirtman BP, Wu Z (2016) Increasing flooding hazard in coastal communities due to rising sea level: case study of Miami Beach, Florida. OceanCoast Manag 126:1–8. https://doi.org/10.1016/j.ocecoaman.2016.03.002

53. Boak EH, Turner IL (2005) Shoreline definition and detection: a review. J Coast Res 21(4):688–703. https://doi.org/10.2112/03-0071.1

54. Lélis R, Calliari L (2006) Historical shoreline changes near lagoonal and river stabilized inlets in Rio Grande do Sul state southern Brazil. J Coast Res. 2004(39):301–305

55. Stockdon HF, Doran KS, Sallenger AH (2009) Extraction of lidar-based dune-crest elevations for use in examining the vulnerability of beaches to inundation during hurricanes. J Coast Res 10053(10053):59–65. https://doi.org/10.2112/si53-007.1

56. Pereira PS, Calliari LJ, Holman R, Holland KT, Guedes RMC, Amorin CK, Cavalcanti PG (2011) Video and field observations of wave attenuation in a muddy surf zone. Mar Geol 279(1–4):210–221. https://doi.org/10.1016/j.margeo.2010.11.004

57. Santos MST, Amaro VE, Souto MVS (2011) Metodologia geodésica para levantamento de linha de costa e modelagem digital de elevaçção de praias arenosas em estudos de precisão de geomorfologia e dinâmica costeira. Revista Brasileira de Cartografia 63(5):663–681

58. Goulart ES, Calliari LJ (2013) Medium-term morphodynamic behavior of a multiple sand bar beach. J Coast Res 165(65):1774–1779. https://doi.org/10.2112/si65-300.1

59. Muehe D, Klumb-Oliveira L (2014) Deslocamento da linha de costa versus mobilidade praial. Quat Environ Geosci 5(2):121–124. https://doi.org/10.5380/abequa.v5i2.35884

60. Doyle TB, Woodroffe CD (2018) The application of LiDAR to investigate foredune morphology and vegetation. Geomorphology 303:106–121. https://doi.org/10.1016/j.geomorph.2017.11.005

61. Hesp P (2002) Foredunes and blowouts: initiation, geomorphology and dynamics. Geomorphology 48(1–3):245–268. https://doi.org/10.1016/S0169-555X(02)00184-8

62. Battiau-Queney Y, Billet JF, Chaverot S, Lanoy-Ratel P (2003) Recent shoreline mobility and geomorphologic evolution of macrotidal sandy beaches in the north of France. Mar Geol 194(1–2):31–45. https://doi.org/10.1016/S0025-3227(02)00697-7

63. Florinsky IV (2017) An illustrated introduction to general geomorphometry. Prog Phys Geogr 41(6):723–752. https://doi.org/10.1177/0309133317733667

64. Li Z, Zhu Q, Gold C (2005) Digital terrain modeling: principles and methodology. CRC Press, Boca Raton, pp 267–284

65. Pike RJ, Evans IS, Hengl T (2009) Geomorphometry: A Brief Guide. In: Hengl T, Reuter HI (eds) Geomorphometry: concepts, software, applications. Elsevier, Amsterdam, pp 141–170

66. Poppenga SK, Worstell BB (2016) Hydrologic connectivity: quantitative assessments of hydrologic-enforced drainage structures in an elevation model. J Coast Res SI 76:90–106. https://doi.org/10.2112/SI76-009

67. Paprotny D, Terefenko P (2017) New estimates of potential impacts of sea level rise and coastal floods in Poland. Nat Hazards Earth Syst Sci 85(2):1249–1277. https://doi.org/10.1007/s11069-016-2619-z

68. Poppenga S, Worstell B (2015) Evaluation of airborne Lidar elevation surfaces for propagation of coastal inundation: the importance of hydrologic connectivity. Remote Sens 7(9):11695–11711. https://doi.org/10.3390/rs70911695

69. Uysal M, Toprak AS, Polat N (2015) DEM generation with UAV photogrammetry and accuracy analysis in Sahitler hill. Meas J Int Meas Confed 73:539–543. https://doi.org/10.1016/j.measurement.2015.06.010

70. Woodget AS, Austrums R, Maddock IP, Habit E (2017) Drones and digital photogrammetry: from classifications to continuums for monitoring river habitat and hydromorphology. Wiley Interdiscip Rev Water 4(4):e1222

71. Chen B, Yang Y, Wen H, Ruan H, Zhou Z, Luo K, Zhong F (2018) High-resolution monitoring of Beach topography and its change using unmanned aerial vehicle imagery. Ocean Coast Manag 160:103–116

72. Ravanelli R, Riguzzi F, Anzidel M, Vecchio A, Nigro L, Spagnoli F, Crespi M (2019) Sea level rise scenario for 2100 A.D. for the archaeological site of Motya. Rend Lincei Sci Fis Nat 30:747–757. https://doi.org/10.1007/s12210-019-00835-3

73. Gašparović M, Seletković A, Berta A, Balenović I (2017) The evaluation of photogrammetry-based DSM from low-cost UAV by LiDAR-based DSM. South-East Eur For 8(2):117–125. https://doi.org/10.15177/seefor.17-16

74. CEPAL. Efectos del cambio climático en la costa de América Latina y el Caribe: impactos (2012) Universidad de Cantabria. Instituto de Hidráulica Ambiental. LC/W.484. 118 p

75. National Aeronautics and Space Administration—NASA (2019). Earth-data portal: sea-level Change observation from space.

https://sealevel.nasa.gov/understanding-sea-level/global-sea-level/. Accessed 10 Nov 2019

76. US Army Corps of Engineers—USACE (1984) Shore Protection Manual. Coast Eng. https://doi.org/10.5962/bhl.title.47830

77. Hoover DJ, Odigie KO, Swarzenski PW, Barnard P (2016) Sea-level rise and coastal groundwater inundation and shoaling at select sites in California, USA. J Hydrol Reg Stud 11:234–249. https://doi.org/10.1016/j.ejrh.2015.12.055

78. Rovere A, Stocchi P, Vacchi M (2016) Eustatic and relative sea level changes. Curr Clim Chang Rep 2(4):221–231. https://doi.org/10.1007/s40641-016-0045-7